# Using Geologically Sequestered CO2 to Generate and Store Geothermal Electricity: CO2 Plume Geothermal (CPG)



**Author(s):**
Adams, Benjamin; Saar, Martin O.; Bielicki, Jeffrey M.; Ogland-Hand, Jonathan D.; Fleming, Mark R.

**Publication date:**
2020-08-31

**Permanent link:**
https://doi.org/10.3929/ethz-b-000444911

Paper ID APEN-MIT-2020_215
Applied Energy Symposium: MIT A+B
August 12-14, 2020 • Cambridge, USA

# Using Geologically Sequestered $CO_2$ to Generate and Store Geothermal Electricity: $CO_2$ Plume Geothermal (CPG)

Benjamin M. Adams
*Dept. of Earth Sciences*
*ETH Zurich*
Zurich, Switzerland
badams@ethz.ch

Martin O. Saar
*Dept. of Earth Sciences*
*ETH Zurich*
Zurich, Switzerland
saarm@ethz.ch

Jeffrey M. Bielicki
*Dept. of Civil, Environmental, and Geodetic Engineering*
*John Glenn College of Public Affairs*
*The Ohio State University*
Columbus, OH, U.S.A.
bielicki.2@osu.edu

Jonathan D. Ogland-Hand
*Dept. of Earth Sciences*
*ETH Zurich*
Zurich, Switzerland
johand@ethz.ch

Mark R. Fleming
*Dept. of Mechanical Engineering*
*Milwaukee School of Engineering*
Milwaukee, WI, U.S.A.
fleming@msoe.edu

*Abstract*—$CO_2$ Plume Geothermal (CPG) is a carbon neutral renewable electricity generation technology where geologic $CO_2$ is circulated to the surface to directly generate power and then is reinjected into the deep subsurface. In contrast to traditional water geothermal power generation with an Organic Rankine Cycle (ORC), CPG has fewer system inefficiencies and benefits from the lower viscosity of subsurface $CO_2$ which allows power generation at shallower depths, lower temperatures, and lower reservoir transmissivities.

In this paper, we modify our existing geothermal electricity models by: 1) replacing TOUGH2 reservoir simulations with analytic solutions for a 5-spot reservoir impedance, and 2) including heat loss to the surrounding rock using a semi-analytical heat transfer solution. We report the results of 3050 simulations in a single plot, showing the power generation of both direct CPG systems and indirect water geothermal systems for depths between 1 and 7 km and reservoir transmissivities between $10^2$ and $10^5$ mD-m ($10^{-13}$ and $10^{-10}$ $m^3$).

*Keywords—$CO_2$ Geothermal; Sedimentary Geothermal Electricity; Porous Media Analytical Solution; Geologic $CO_2$; Carbon Capture Utilization and Storage (CCUS); Enhanced Geothermal Systems (EGS); $CO_2$ Plume Geothermal (CPG); Electric Power Generation*

## 1 Introduction

$CO_2$ Plume Geothermal (CPG) is a $CO_2$-based geothermal electricity generation system which utilizes sequestered $CO_2$ in sedimentary basins [1]. CPG can generate more electricity than traditional water geothermal at moderate depths (>2 km) and permeabilities (~>20 mD) due to the low viscosity of supercritical $CO_2$ at these conditions [2,3]. As geothermal energy is not a variable energy source like wind and solar, CPG can generate either dispatchable or baseload carbon-neutral electricity, and can be modified to provide energy storage [4-6].

A $CO_2$ Plume Geothermal (CPG) facility is built at an established $CO_2$ sequestration site. $CO_2$ will likely be sequestered in large quantities in the future as a part of climate change mitigation [7]. Once sequestered geologically, the $CO_2$ can enable the extraction of geothermal heat, making CPG a Carbon Capture Utilization and Storage (CCUS) technology. This can provide a return on the $CO_2$ capture and sequestration costs.

In [2], the power generated for both CPG and water geothermal was found for depths between 1 and 5 km, permeabilities between 1 and 1000 mD, geothermal gradients between 20 and 50 °C/km, and pipe diameters between 0.14 and 0.41 m. While we focused on permeability as a primary reservoir variable in [2], we have since determined that the reservoir transmissivity, which is the product of permeability and thickness, is the more important quantity. This does not affect our results in [2], as they were found with a constant reservoir thickness, but reporting results as a function of transmissivity, rather than permeability, would have been more representative of the system physics. Thus, we report our results primarily as a function of reservoir transmissivity here.

In [2], we used a TOUGH2 reservoir simulator to calculate the reservoir impedance, which is the difference between the injection and production well downhole pressures divided by the mass flowrate. This added substantial complexity to the model, ultimately resulting in the characterization of numerous TOUGH2 simulation results. Additionally, the TOUGH2 results showed little or no thermal depletion after the first year. Thus, we have since replaced the TOUGH2 simulations in our CPG model with an analytical solution for reservoir impedance with a constant reservoir production temperature. This simplification is employed herein.

Lastly, the wellbore simulations in [2] neglect the conduction of heat to and from the surrounding rock. We showed in [8] that this heat loss reduces the wellhead

temperature by less than 5% after two weeks at the high flow rates used in CPG. Thus, the adiabatic wellbore assumption was justified. However, the wellhead temperature due to heat loss varies proportionally with the wellbore mass flowrate [9], i.e. decreasing the mass flowrate also decreases the wellhead temperature. Therefore, at some flowrates lower than those used in CPG, the adiabatic assumption may not be justified. Thus, we have additionally included a semi-analytic heat transfer relation into our wellbore model to alleviate uncertainty and to provide robust results in all scenarios.

In this paper, we find the power generation of both direct CPG and indirect water geothermal systems for depths between 1 and 7 km, and transmissivities between 100 and 100,000 mD-m. We also describe an analytical reservoir model using Darcy's law and an enhanced wellbore model accounting for conduction heat losses. These modifications make it possible to generate large, parameter space results.

## 2 Methods

Both a direct CPG system and an indirect water geothermal system are shown in Figure 1.

In a CPG system (Figure 1A), the $CO_2$ is injected at the surface in liquid form (State 1) and arrives at the reservoir as supercritical $CO_2$ (State 2). Through the reservoir, the $CO_2$ is heated and decreases in pressure according to Darcy's Law, arriving at State 3 where the pressure is hydrostatic and the temperature is the product of the geothermal gradient and depth plus the surface average ambient temperature. The $CO_2$ rises to the wellhead (State 4), where the pressure is much greater than the liquid injection temperature (State 7), due to the low production well density [3]. The $CO_2$ pressure differential across the turbine results in generated power. The turbine backpressure (State 5) is the condensing pressure of $CO_2$ at the ambient temperature plus the approach temperature (i.e. ~6 MPa at 22°C). The $CO_2$ is condensed sub-critically to a saturated liquid at State 7. The $CO_2$ is pumped to State 1, increasing the circulating mass flowrate, though pumping is not necessary and the $CO_2$ will self-circulate without pumps due to the thermosiphon [2,3].

In a direct water geothermal system (Figure 1B), a similar process occurs. The reservoir pressure change is still calculated according to Darcy's Law. However, water is incompressible, therefore its density in both the production and injection wells are roughly equal. Thus, the water pressure reduces more quickly with increasing depth than $CO_2$, and a downhole pump is required to keep the water pressure above its boiling point. Similarly, the water pressure is much lower at the surface in the indirect system, and energy is extracted as heat instead. The heat drives an Organic Rankine Cycle (ORC). We use R245fa as the ORC working fluid; however we have also used $CO_2$ [2].

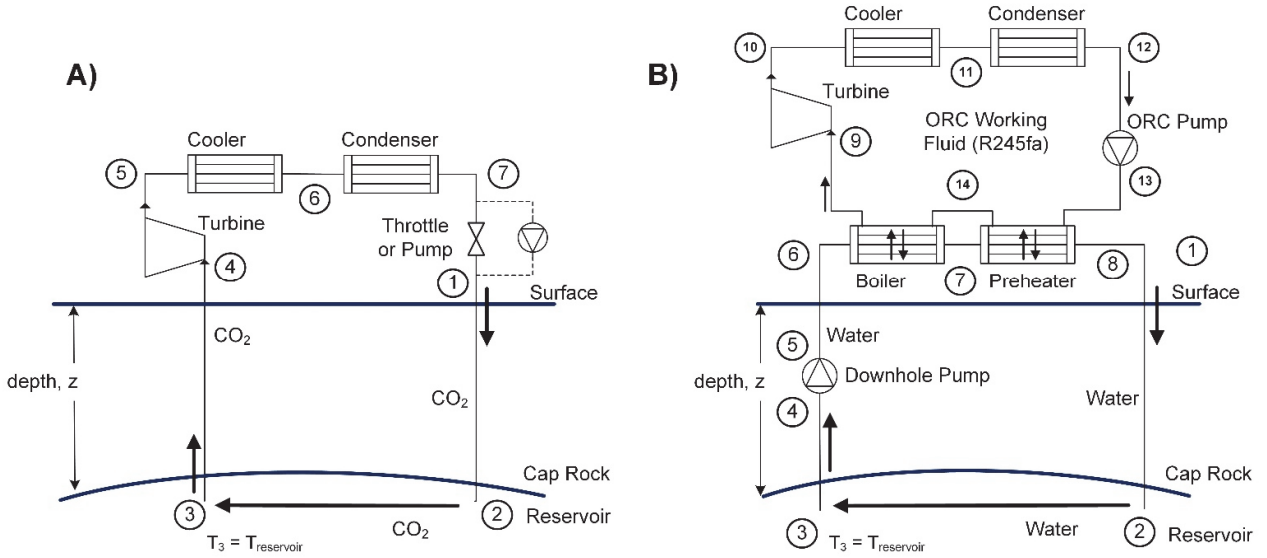


Fig. 1. Cycle schematics for A) direct CPG and B) indirect water Organic Rankine Cycle (ORC), modified from [2].

The direct CPG and indirect water thermodynamic models used in this analysis are the same as was used in [2], with the following changes: 1) The TOUGH2 simulator is replaced with a Darcy analytical solution, and 2) conduction heat loss is included in the wellbore. These changes are described in Sections 2.1 and 2.2.

Both the direct CPG and indirect water power cycle models were rebuilt in MATLAB. The key simulation parameters are given in Table 1.

Offline simulations have found that large pipe diameters are worth the increased cost, thus we only simulate 0.41 m diameter wells here. Also, we found in [2] that the 20 °C/km systems often provide little power and geologic locations with a geothermal temperature gradient of 50 °C/km are difficult to find. Thus, we assume a 35 °C/km geothermal gradient for all simulations in this paper.

TABLE I. Model Assumptions

| *Parameter* | *Value* |
|---|---|
| Geologic Temperature Gradient | 35 °C/km |
| Reservoir Pressure | Hydrostatic |
| Well Diameter | 0.41 m |
| Surface Temperature | 15 °C |
| Tower Approach Temperature | 7 °C |
| Well Roughness | 55 μm |
| Well Pattern | 1 $km^2$ Inverted 5-spot |
| Primary Geothermal Fluid | $CO_2$ or Water |
| Secondary ORC Fluid (Water Only) | R245fa |

*2.1 Darcy Analytical Solutions*

In [2], TOUGH2 was used to simulate the reservoir impedance and temperature depletion. We have since found that with 707 well spacing, the same as in the inverted 5-spot pattern used for the simulations in this paper, the temperature does not deplete substantially for at least 20 or 30 years [10,11]. As we are chiefly interested in the first decade of power generation, we assume the production temperature of the reservoir is equivalent to the initial reservoir temperature. The initial reservoir temperature is the product of geologic temperature and depth plus the surface temperature. Similarly, we have found that the reservoir impedance can be estimated as accurately as TOUGH2, but more quickly using an analytical solution.

We provide three analytical solutions here: a square, 5-spot well pattern (Section 2.1.1), a concentric circle approximation of a source-sink pair (Section 2.1.2), and a more exact solution for a source-sink pair using a potential function (Section 2.1.3). A source-sink pair is a source and sink spaced a non-zero distance apart, i.e. an injection and production well pair. We only use 5-spot reservoirs within the results reported in Section 3, but the others are reported for comparison. Note that a "source-sink pair" is commonly referred to as a "doublet" within the geothermal community; however, these have different meanings within fluid dynamics, thus the term "doublet" is avoided here.

*2.1.1 5-spot Analytical Solution*

The one-dimensional Darcy equation can be expressed in Equation 1, where $P$ is the pressure, $\mu$ is the dynamic viscosity of the fluid, $V$ is the Darcy velocity, $\kappa$ is the permeability, and x is distance in the direction of fluid flow.

$$dP = -\frac{\mu \cdot V}{\kappa} dx \tag{1}$$

The continuity equation is shown in Equation 2, where the mass flowrate, $\dot{m}$, is equal to the product of fluid density, $\rho$, cross-sectional area, $A_c$, and fluid velocity, $V$.

$$\dot{m} = \rho \cdot A_c \cdot V \tag{2}$$

Equation 2 is substituted into Equation 1, yielding Equation 3.

$$dP = -\frac{\mu}{\rho} \frac{\dot{m}}{\kappa \cdot A_c} dx \tag{3}$$

For a one-quarter domain of a 5-spot configuration, the x-axis is aligned on a line between the injection and production wells. The cross-sectional area, $A_c$, along this line from the well to the midpoint is given in Equation 4, where $b$ is the reservoir thickness.

$$A_c = 2 \cdot x \cdot b \tag{4}$$

Combining Equations 3 and 4 and integrating from the well perimeter to the midpoint is given in Equation 5, where $x_0$ is the well boundary location and $L$ is the distance between the injection and production wells. Integration yields Equation 6, where $\Delta P$ is the pressure decrease from the well to the midpoint.

$$\int dP = -\frac{\mu}{\rho} \frac{\dot{m}}{2 \cdot \kappa \cdot b} \int_{x_0}^{\frac{L}{2}} \frac{1}{x} dx \tag{5}$$

$$\Delta P = \frac{\bar{\mu}}{\bar{\rho}} \frac{\dot{m}}{2 \cdot \kappa \cdot b} \ln\left(\frac{L}{2 \cdot x_0}\right) \tag{6}$$

The pressure decrease for the entire well spacing, $L$, is found by doubling Equation 6. The viscosity, $\bar{\mu}$, and density, $\bar{\rho}$, are effective values within the entire reservoir. Also, the well perimeter in this one-dimensional Cartesian space is a square, where each segment has a length of $2 \cdot x_0$. Thus, equating the perimeter of a circle with diameter, $D$, and a square with the same perimeter yields Equation 7.

$$\pi \cdot D = 4 \cdot (2 \cdot x_0) \tag{7}$$

$$\frac{\Delta P}{\dot{m}} = \frac{\bar{\mu}}{\bar{\rho}} \frac{1}{\kappa \cdot b} \ln\left(\frac{4 \cdot L}{\pi \cdot D}\right) \tag{8}$$

Substitution yields the reservoir impedance, $\Delta P / \dot{m}$, in Equation 8 as a function of well diameter, $D$. This is valid for all quadrants within a 5-spot reservoir. Note that the reservoir impedance is inversely proportional to the reservoir transmissivity, $\kappa b$, which is the product of reservoir permeability and thickness.

*2.1.2 Source-sink Circular Analytical Solution*

A similar approach may be used to solve for the reservoir impedance of a source-sink pair. In this approximation, we assume the flow between the source and sink flows uniformly and radially in all directions, up to a radius of $L/2$. For this source-sink pair, we use radial space and substitute $dx = dr$ in Equation 1. The cross-sectional area of flow is the product of the circumference at that distance and the reservoir thickness, given in Equation 9.

$$A_c = 2 \cdot \pi \cdot r \cdot b \tag{9}$$

By combining Equations 3 and 9, we obtain Equation 10, where $r_0$ is the well radius. Integration yields Equation 11 which is the pressure difference from the well to the midpoint.

$$\int dP = -\frac{\mu}{\rho} \frac{\dot{m}}{2 \cdot \pi \cdot \kappa \cdot b} \int_{r_0}^{\frac{L}{2}} \frac{1}{r} dr \tag{10}$$

$$\Delta P = \frac{\bar{\mu}}{\bar{\rho}} \frac{\dot{m}}{2 \cdot \pi \cdot \kappa \cdot b} \ln\left(\frac{L}{2 \cdot r_0}\right) \tag{11}$$

Equation 11 is rearranged into the reservoir impedance of an approximate source-sink pair in Equation 12, where the well radius is half the well diameter.

$$\frac{\Delta P}{\dot{m}} = \frac{\bar{\mu}}{\bar{\rho}} \frac{1}{\pi \cdot \kappa \cdot b} \ln\left(\frac{L}{D}\right) \tag{12}$$

Note that for large values of $L/D$, the reservoir impedance of Equation 12 differs from the reservoir impedance of a 5-spot (Equation 8) by a factor of $\pi$. Additionally, in a 5-spot, the mass flowrate in the central injection well is four times greater than the mass flowrate in any of the quadrants. Therefore, for the same injection well mass flowrate, the source-sink domain mass flowrate is four times larger than the 5-spot quadrant mass flowrate and the reservoir pressure difference then only differs by a factor of $4/\pi$. This 27% difference is due to the 27% smaller swept area of the source-sink in this approximation. Thus, in Section 2.1.3, we use the potential functions to include the entirety of the reservoir area.

*2.1.3 Source-sink Potential Analytical Solution*

The pressure potential curve surrounding a source or sink does not have a constant radius, as is assumed in the earlier approximation. Thus, to gain a more precise solution, we integrate the distance of the potential curve surrounding the sink to obtain the cross-sectional area, given in Equation 13, where $r_1$ is the radius to the equipotential line from the sink and $\theta$ is the inclination.

$$A_c = b \cdot \int_0^{2\pi} r_1 \, d\theta \tag{13}$$

For source-sink potential flow, the stream potential, $\varphi$, is given by Equation 14, where $M$ is the source-sink strength, $r_1$ is the radial distance from the sink and $r_2$ is the radial distance from the source [12].

$$\varphi = -\frac{M}{2\pi} \ln\left(\frac{r_1}{r_2}\right) \tag{14}$$

On the shortest streamline which extends directly from the sink to source, the potential is Equation 15, evaluated where $r_1 = r$ and $r_2 = L - r$ along this streamline, where L is the distance between the sink and source.

$$\varphi = -\frac{M}{2\pi} \ln\frac{r}{L-r} \tag{15}$$

Equating Equations 14 and 15, yields Equation 16, which provides the distances $r_1$ and $r_2$ along a line of constant potential as a function of $L$ and $r$. Equation 16 is solved for $r_2^2$ in Equation 17.

$$\frac{r_2}{r_1} = \frac{L}{r} - 1 \tag{16}$$

$$r_2^2 = r_1^2 \cdot \left(\frac{L}{r} - 1\right)^2 \tag{17}$$

Separately, we find length $r_2$ as a function of $r_1$ and $\theta$ in Equation 18 using trigonometry.

$$r_2^2 = r_1^2 + L^2 - 2 \cdot L \cdot r_1 \cdot \cos\theta \tag{18}$$

Equating Equations 17 and 18, solving for $r_1$, integrating according to Equation 13, and assuming large values of $L$ (i.e. $L \gg 1$) yields Equation 19.

$$A_c = \frac{2 \cdot \pi \cdot b}{\left(\frac{1}{r^2} - \frac{2}{L \cdot r}\right)^{0.5}} \tag{19}$$

The denominator in Equation 19 does not lend itself to simple integration. Thus, we make the approximation of Equation 20. This assumption preserves the anomaly occurring where $r = L/2$ in which the cross-sectional area becomes infinite. At the midpoint between source and sink, the line of equal potential is tangent to streamline, and extends to infinity.

$$\left(\frac{1}{r^2} - \frac{2}{L \cdot r}\right)^{0.5} = \left(\frac{1}{r}\right)^{0.5} \cdot \left(\frac{1}{r} - \frac{2}{L}\right)^{0.5} \approx \left(\frac{1}{r} - \frac{2}{L}\right) \tag{20}$$

Equations 19 and 20 are combined with Equation 3 in radial space ($dx = dr$) and integrated similar to Equation 10. The resulting reservoir impedance is given in Equation 21, where $e$ is Euler's number.

$$\frac{\Delta P}{\dot{m}} = \frac{\bar{\mu}}{\bar{\rho}} \frac{1}{\pi \cdot \kappa \cdot b} \left[\ln\left(\frac{L}{D \cdot e}\right) + \frac{D}{L}\right] \tag{21}$$

Equation 21 is very similar to Equation 12, differing only by the factor of $e$ within the natural logarithm. The factor $D/L$ is comparatively small for large values of $L/D$ and can thus be neglected. For reservoir length to well diameter ratios of 1000 (i.e. $L/D = 1000$), Equation 21 provides a reservoir impedance value approximately 15% smaller than Equation 12. The impedance value decreases to 22% for a ratio of 100. This decreased impedance using the potential flow method is enabled by the infinite reservoir area of the source-sink pair.

Care should be used with all three of these derivations as they are one-dimensional and assume a uniform velocity profile through a cross-sectional area. Thus, they do not account for flow deviations, heterogeneities, or buoyancy. They do, at minimum, provide an order-of-magnitude approximation of the reservoir behavior for use within a geothermal system.

### *2.2 Wellbore Heat Loss*

Heat loss to the rock surrounding the wellbore is implemented using a semi-analytical approach. In each wellbore element that is numerically integrated [2], an analytical heat solution for a semi-infinite solid is applied from [13]. This approach assumes: heat conduction only occurs radially to the far-field and the wellbore wall temperature is constant with time.

Similar to [2], the wellbore elements are evaluated numerically, with pressure (Equation 22) and energy (Equation 23) balances across each element, where $\Delta z$ is the change in element elevation, $\Delta P_{Loss}$ is the pipe frictional loss, $h$ is the enthalpy, $Q_{Loss}$ is the heat exchange to the surroundings, and $\dot{m}$ is the fluid mass flowrate. The pressure loss equation is identical to [2], while the energy equation includes the new heat exchange term.

$$P_{i+1} = P_i - \rho \cdot g \cdot \Delta z - \Delta P_{Loss} \tag{22}$$

$$h_{i+1} = h_i - g \cdot \Delta z - \frac{Q_{Loss}}{\dot{m}} \tag{23}$$

The heat loss is solved using Equation 24 from [13], where $k_{Rock}$ is the thermal conductivity of rock, $\beta$ is a non-dimensional time-dependent factor, $T_w$ is the well wall temperature and $T_e$ is the far-field reservoir temperature at depth equal to the product of geologic temperature gradient and depth plus the average surface temperature. It is assumed that the well casing and fluid heat transfer resistances are small compared to conduction through the rock and are thus neglected.

$$Q_{Loss} = \Delta z \cdot 2 \cdot \pi \cdot k_{Rock} \cdot \beta \cdot (T_w - T_e) \tag{24}$$

The wall temperature is an intermediate temperature between the wellbore fluid temperature and far-field rock temperature. Without any heat loss, the wellbore elements are assumed to be sufficiently long that the fluid temperature is in thermal equilibrium with the well wall. Thus, $T_w$ is assumed to be the resulting fluid temperature for an enthalpy of $h_i$ and pressure of $P_i$ if the heat loss term in Equation 23 were zero.

The dimensionless factor beta is given by [13] as Equation 25, where $t_d$ is the dimensionless time.

$$\beta = \begin{cases} (\pi \cdot t_d)^{-0.5} + \frac{1}{2} - \frac{1}{4}\left(\frac{t_d}{\pi}\right)^{0.5} + \frac{1}{8} t_d, & t_d \le 2.8 \\ \frac{2}{ln(4 \cdot t_d) - 1.16} - \frac{1.16}{(ln(4 \cdot t_d) - 1.16)^2}, & t_d > 2.8 \end{cases} \tag{25}$$

The dimensionless time, $t_d$, is given in Equation 26, where $\rho_{Rock}$ is the rock density, $c_{Rock}$ is the rock specific heat, and $t$ is the time.

$$t_d = \frac{k_{Rock}}{\rho_{Rock} \cdot c_{Rock}} \frac{4 \cdot t}{D^2} \tag{26}$$

## 3 Results and Discussion

Using the updated wellbore and reservoir models described here, we obtained the results of Figure 2 for both $CO_2$ and water as geologic working fluids. The results are for a geologic temperature gradient of 35 °C/km, depths of 1 to 7 km, and reservoir transmissivities of $10^2$ to $10^5$ mD-m ($10^2$

mD-m = $10^{-13}$ $m^3$). The reservoir transmissivity of a porous medium is the product of permeability and thickness. Figure 2 is a contour plot generated from 3050 individual simulations. In each simulation, a mass flowrate was used which maximizes the power generated. The fuchsia star indicates the power generated for the base-case of [2], a 2.5 km deep reservoir with 50 mD permeability and 300 m thickness (i.e. $\kappa b = 15\,000$ mD-m).

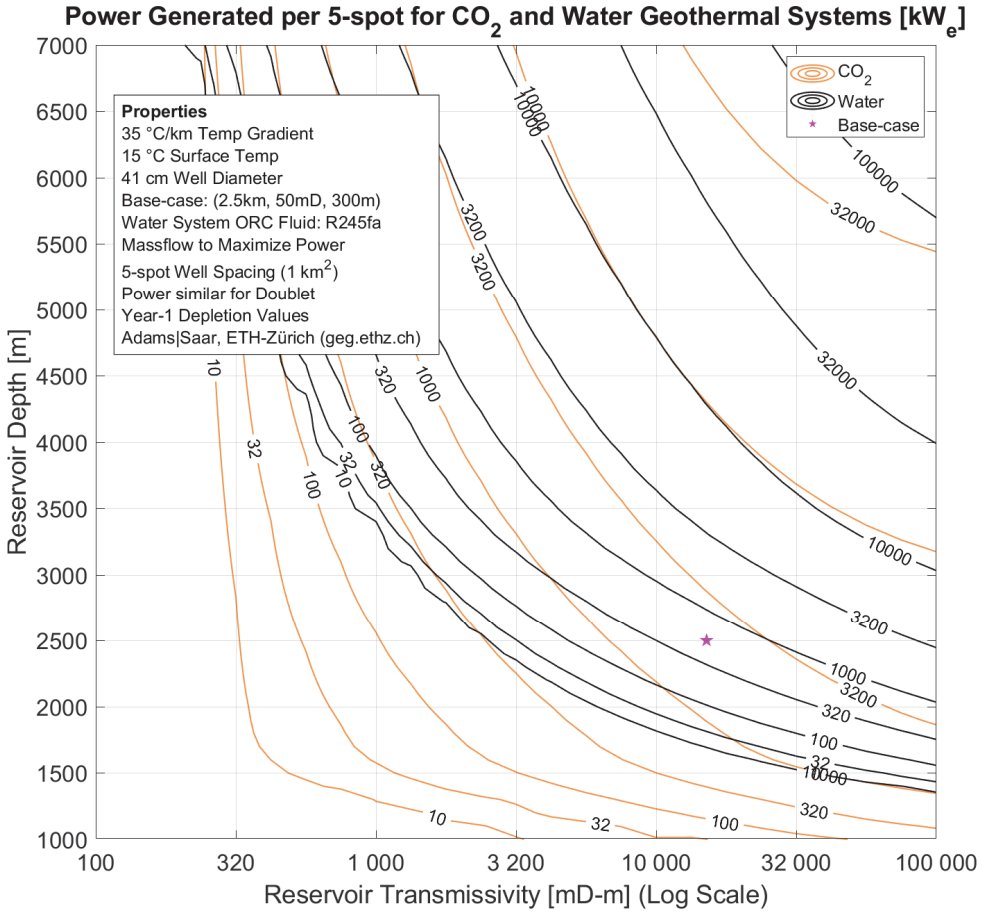


Fig. 2. Power generated per 5-spot for $CO_2$ and water geothermal systems as a function of reservoir depth and transmissivity. A 35 °C/km geologic temperature gradient is assumed. The fuchsia star indicates the power generated for the base-case: a 2.5 km reservoir with 300m thickness and 50 mD permeability (i.e. 15,000 mD-m transmissivity).

Figure 2 shows that a direct CPG system can generate power at shallower depths and lower transmissivities than an indirect water system. If a power threshold minimum of 100 $kW_e$ is selected, a CPG system generates power for reservoirs as shallow as 1 km with transmissivities of approximately 32,000 mD-m. Similarly, a 3 km reservoir with a transmissivity of approximately 900 mD-m also generates 100 $kW_e$ of electricity. Conversely, at a 3 km depth, the water geothermal system requires a half-order of magnitude larger transmissivity to generate 100 $kW_e$, and there is no water geothermal system which will generate electricity at a depth of 1 km under these conditions.

Power generation at shallow depths with the direct $CO_2$ system is possible due to two factors. 1) The viscosity of $CO_2$ is much lower than water at these depths and temperatures, resulting in low reservoir impedance which reduces the energy required to extract heat from the reservoir. 2) More importantly, power generation with water geothermal using an ORC fundamentally requires the transfer of thermal energy at the surface to a second power cycle. Given the low resource temperature of a 1 km system, the heat transfer inefficiencies result in little heat to drive the Rankine cycle. Conversely, in a direct CPG system, the subsurface heat addition in the reservoir and subsequent turbine and heat removal at the surface in-and-of-themselves constitute a Rankine cycle. Thus, the exergy does not need to be transferred (and lost) to a second system to generate electricity. This is a chief benefit of a CPG system—the reservoir is part of the Rankine cycle, simplifying the system and reducing the inefficiencies.

Power generation increases with depth and transmissivity. This finding is consistent with our previous work [2], but is more directly illustrated here. In Figure 2, both the $CO_2$ and water geothermal systems increase toward the upper-right corner. At low depth and transmissivity, the direct $CO_2$ system generates more power. However, at a power generation contour of approximately 10 $MW_e$, the water geothermal system begins to generate more power. At these depths and transmissivities, the low viscosity advantage of $CO_2$ is diminished and supplanted by the high specific heat of water. Water is simply an excellent transporter of heat.

## 4 Concluding Remarks

In this work, we have shown our evolution in simulating both water and $CO_2$ geothermal systems. We have shown two first-principle improvements that have reduced computational time to permit generation of large datasets: replacing the TOUGH2 reservoir model with a Darcy analytical solution and adding heat loss to surrounding rock within the wellbore. These improvements, especially the Darcy solution, have provided insight into the governing relations of our geothermal models. For instance, we now report all results as a function of transmissivity, rather than permeability, as this is the primary driver of reservoir pressure loss.

In a perfect world, one could select the ideal geologic fluid to suit any specific site. However, the choice of $CO_2$ or water for a site will probably not depend on geothermal power generation. $CO_2$ will likely be sequestered for climate change reasons and the injection of $CO_2$ at a site purely for geothermal reasons is not financially feasible. Thus, when presented with a site with an established subsurface fluid, Figure 2 will help in estimating the geothermal electricity generation potential.

Lastly, the modeling and analysis here are only part of an ongoing effort to model geothermal energy generation within the Geothermal Energy and Geofluids (GEG) group at ETH Zurich. We continue to refine our models, and are working towards including cost and financing assumptions for future reporting.

## Acknowledgment

We thank the Werner Siemens Foundation (Werner Siemens-Stiftung) for its support of the Geothermal Energy and Geofluids (GEG) Group at ETH Zurich, Switzerland. BMA thanks his colleagues in the Geothermal Energy and Geofluids Group at ETH Zürich, in particular: Dr. Samrock, Dr. Kyas, Dr. Birdsell, Dr. Vogler, Dr. Niederau, and Dr. Schädle for their thoughtful feedback and constructive criticism. BMA additionally thanks Dr. Ebigbo at Helmut Schmidt University for his generous time contribution and consultation regarding the reservoir impedance derivations.

ACT ELEGANCY, Project No 271498, has received funding from DETEC (CH), FZJ/PtJ (DE), RVO (NL), Gassnova (NO), BEIS (UK), Gassco AS and Statoil Petroleum AS, and is cofounded by the European Commission under the Horizon 2020 programme, ACT Grant Agreement No 691712.

## References

[1] Randolph, J.B. & Saar, M.O. (2011). Combining geothermal energy capture with geologic carbon dioxide sequestration. *Geophysical Research Letters*, 38, L10401. https://dx.doi.org/10.1029/2011GL047265

[2] Adams, B.M., Kuehn, T.H., Bielicki, J.M., Randolph, J.B., & Saar, M.O. (2015). A comparison of electric power output of $CO_2$ Plume Geothermal (CPG) and brine geothermal systems for varying reservoir conditions. *Applied Energy*, 140, 365-377. https://doi.org/10.1016/j.apenergy.2014.11.043

[3] Adams, B.M., Kuehn, T.H., Bielicki, J.M., Randolph, J.B., & Saar, M.O. (2014). On the importance of the thermosiphon effect in CPG ($CO_2$ plume geothermal) power systems. *Energy*, 69, 409-418. https://doi.org/10.1016/j.energy.2014.03.032

[4] Fleming, M.R., Adams, B.M., Randolph, J.B., Ogland-Hand, J.D., Kuehn, T.H., Buscheck, T.A., Bielicki, J.M., & Saar, M.O. (2018). High efficiency and large-scale subsurface energy storage with CO2. *Proceedings, 43rd Workshop on Geothermal Reservoir Engineering, Stanford University, Stanford, CA, February 12-14, 2018*.

[5] Adams, B.M., Fleming, M.R., Bielicki, J.M., Hansper, J., Glos, S., Langer, M., Wechsung, M., & Saar, M.O. (2019). Grid scale energy storage using $CO_2$ in sedimentary basins: The cost of power flexibility. *European Geothermal Congress*, Hague, Netherlands, 11-14 June, 2019.

[6] Fleming, M.R., Adams, B.M., & Saar, M.O. (Accepted, 2021). Using sequestered $CO_2$ as geothermal working fluid to generate electricity and store energy. *World Geothermal Congress*, Reykjavik, 21 May to 26 May, 2021.

[7] IPCC. (2005). IPCC special report on carbon dioxide capture and storage. Prepared by working group III of the Intergovernmental Panel on Climate Change [Metz, B., Davidson, O., deConinck, H.C., Loos, M., and Meyer, L.A. (eds.)]. Cambridge University Press, Cambridge, New York.

[8] Randolph, J.B., Adams, B., Kuehn, T.H., & Saar, M.O. (2012) Wellbore heat transfer in $CO_2$-based geothermal systems. *Geothermal Resources Council Transactions*, 36: 549-554.

[9] Ramey, Jr., H.J. (1962). Wellbore Heat Transmission. Society of Petroleum Engineers.

[10] Garapati, N., Randolph, J.B., & Saar, M.O. (2015). Brine displacement by $CO_2$, energy extraction rates, and lifespan of a $CO_2$-limited $CO_2$-plume geothermal (CPG) system with a horizontal production well. *Geothermics*, 55, 182-194.

[11] Adams, B.M., Vogler, D., Kuehn, T.H., Bielicki, J.M., Garapati, M., & Saar, M.O. (submitted). Heat depletion in sedimentary basins and its effect of the design and electric power output of $CO_2$ plume geothermal (CPG) systems. *Renewable Energy*.

[12] Stern, F. (2006). 57:020 Mechanics of fluids and transport processes lecture notes. https://user.engineering.uiowa.edu/~fluids/Posting/Lecture_Notes/Chapter6_Potential_Flow.pdf

[13] Zhang, Y., Pan, L., Pruess, K., & Finsterle, S. (2011). A time-convolution approach for modelling heat exchange between a wellbore and surrounding formatioon. *Geothermics*, 40, 261-266.